This is a repository copy of *Order and disorder in cerium-rich ceria-zirconia solid solutions revealed from reverse Monte Carlo analysis of neutron and x-ray total scattering*.

White Rose Research Online URL for this paper:
https://eprints.whiterose.ac.uk/207588/

Version: Published Version

eprints@whiterose.ac.uk
https://eprints.whiterose.ac.uk/

RESEARCH ARTICLE | MARCH 21 2023

Order and disorder in cerium-rich ceria-zirconia solid solutions revealed from reverse Monte Carlo analysis of neutron and x-ray total scattering ⓕ

Aron Summer ⓘD ; Helen Y. Playford ⓘD ; Lewis R. Owen ⓘD ; Janet M. Fisher; Amy Kolpin; David Thompsett; Richard I. Walton ✉ ⓘD

Check for updates

View Online   Export Citation   CrossMark

Order and disorder in cerium-rich ceria-zirconia solid solutions revealed from reverse Monte Carlo analysis of neutron and x-ray total scattering

Aron Summer,[1] (ID) Helen Y. Playford,[2] (ID) Lewis R. Owen,[3] (ID) Janet M. Fisher,[4] Amy Kolpin,[4] David Thompsett,[4] and Richard I. Walton[1,a)] (ID)

AFFILIATIONS

[1] Department of Chemistry, University of Warwick, Gibbet Hill Road, Coventry CV4 7AL, United Kingdom
[2] ISIS Neutron and Muon Source, Rutherford Appleton Laboratory, Didcot OX11 0QX, United Kingdom
[3] Department of Materials Science and Engineering, University of Sheffield, Sir Robert Hadfield Building, Mappin Street, Sheffield S1 3JD, United Kingdom
[4] Johnson Matthey Technology Centre, Blounts Court, Sonning Common, Reading RG4 9NH, United Kingdom

Note: This paper is part of the Special Topic on Challenges and Perspectives in Materials Chemistry—A Celebration of Professor Sir Anthony K. Cheetham's 75th Birthday.
[a)]Author to whom correspondence should be addressed: r.i.walton@warwick.ac.uk

ABSTRACT

A reverse Monte Carlo analysis of neutron and x-ray total scattering data from two ceria-zirconia samples of composition $Ce_{0.75}Zr_{0.25}O_2$ is performed to analyze the distribution of cations and to examine the possibility of oxide-ion disorder. For the first material, heated in air under moderate conditions ($800\,°C$), the structure is a single-phase solid-solution with the statistical distribution of cations, but a local tetragonal symmetry is found, consistent with the different coordination preferences of Ce and Zr. For the second material, heated under H_2 at $1050\,°C$ followed by reoxidation at $400\,°C$, the structure shows a considerable disorder, with evidence for oxygen interstitials (Frenkel-ion defects) and a non-statistical distribution of cations with significantly higher concentrations of like–like cation nearest neighbors, highlighting the existence of cation-rich nano-domains. The results highlight the dynamic nature of this solid-solution, with structural evolution upon thermal treatment, which is of relevance to understanding its stability under redox catalytic conditions in practical applications.

I. INTRODUCTION

Mixed oxides of cerium and zirconium have long attracted attention because of their use in heterogeneous catalysis.[1] These applications utilize considerable oxide-ion mobility in the solid state coupled with reversible redox chemistry between Ce^{4+} and Ce^{3+}, together giving an oxygen storage capacity.[2] Most notably, this is put to use in the three-way catalytic converter for remediation of polluting emissions from the combustion engine,[3] but oxides of cerium have an extensive range of catalysis applications where they are commonly used as a support for precious metals, including in water–gas shift,[4] steam reforming,[5] oxidation of volatile organics,[6] soot oxidation,[7] and thermochemical water splitting.[8] The defect chemistry of CeO_2 (ceria) itself is well known to be important in tuning its properties,[9] while the role of zirconium is to replace Ce^{4+} with an isovalent cation without lowering the oxide content and to give a local distortion in the structure due to the size mismatch of the ions that introduces a high lattice strain: this is established to be the origin of enhanced oxygen storage capacity and is accompanied by enhanced thermal stability.[10]

The replacement of Ce^{4+} by Zr^{4+} is one of the most widely studied substitutions used to tune the properties of ceria, and a

ceria–zirconia phase diagram is well established. A complete substitutional series, $Ce_{1-x}Zr_xO_2$, is possible from cubic cerium-rich compositions with x < 0.5, to tetragonal zirconium-rich phases with x > 0.5, and to monoclinic for the most zirconium-rich materials, x > 0.88.[2] These are equilibrium crystal structures for materials prepared at high temperatures, and an effect of crystallite size on the stability of various phases has been proposed. It should be noted that any degree of tetragonality may be small for x < 0.5 and can also be difficult to detect when a diffraction profile is broadened due to the small crystal domain size, giving rise to pseudo-cubic materials.[11] A phase separation on extended heat treatment may take place,[12] and conceivably, the local atomic arrangements of cations may evolve with use, where samples are exposed to conditions ranging from oxidative to reductive at elevated temperatures. The operating temperature in a catalytic converter is typically 400–600 °C and commonly reaches higher values.[13]

Analysis of the onset of phase separation in solid solutions of oxides requires techniques beyond the conventional analysis used in the laboratory, and the analysis of pair distribution functions (PDFs) is becoming an established method for probing issues around local vs long-range order, making use of scattering data measured across a wide range of momentum transfer, which, when Fourier transformed, yields radial distribution functions that contain information about all atomic pairs, irrespective of any crystal symmetry.[14] The method is especially powerful when the PDF is analyzed alongside the Bragg diffraction to yield a structural model that reconciles short-range and long-range order, so-called total-scattering analysis. Previous PDF studies of cerium oxide and cerium–zirconium mixed oxides have been reported in the literature. Most of these works use a crystal-structure-based analysis to build models that match the measured PDF, with refinement of atomic displacements to optimize the fit. For example, Mamontov and Egami studied CeO_2 using neutron-derived PDFs and detected the presence of interstitial oxygens that were removed upon annealing at high temperatures.[15] In the case of Y- and Gd-substituted ceria, Ferrero and co-workers used the PDF method to show that the local environment of the mixed oxides could be reconciled using biphasic models, reflecting the different coordination preferences of the two cations.[16,17] The reverse Monte Carlo (RMC) method, which produces large-box atomistic models without explicit symmetry constraints,[18,19] has previously been applied to PDFs derived for pure CeO_2. This includes a highly crystalline sample with little deviation from the average structure,[20] a material whose oxide-ion defects were found to be preferentially clustered,[21] and a nanoparticulate sample where the box used for modeling could simulate the concentration of defects at the surface.[22] In the case of ceria–zirconia, Mamontov et al. studied a sample of composition $Ce_{0.5}Zr_{0.5}O_2$ using neutron PDFs and concluded that the material consisted of ~25–30 Å domains of $Ce_{0.4}Zr_{0.6}O_2$ in a matrix of $Ce_{0.7}Zr_{0.3}O_2$.[23]

In this paper, we take the analysis of cerium-rich ceria-zirconia materials to a higher level of detail than previously reported, using RMC analysis to examine issues of both oxide disorder and cation segregation, as well as the deviation from the highly symmetrical fluorite structure. In the case of cation distribution over the average face-centered cubic lattice, we use a statistical Clapp configuration analysis (previously adopted for binary metallic alloys)[24,25] to explore the occurrence of preferred arrangements of Ce and Zr.

Two samples are studied, produced by taking an identical material and heating it under two different conditions.

II. EXPERIMENTAL DETAILS
A. Samples

The material with composition $Ce_{0.75}Zr_{0.25}O_2$ was provided by Johnson Matthey and was then treated under two different conditions. One sample was prepared by heating in air at 800 °C, while the second was treated with high temperature reduction at 1050 °C for 4 h under a reducing atmosphere using pure H_2 gas, followed by a mild oxidation at 400 °C in air for 2 h. This reduction–oxidation was chosen to mimic the conditions of temperature programmed reduction under hydrogen, which is used to assess redox properties.

B. Neutron total scattering

Neutron total scattering data were acquired on the Polaris instrument beamline at the STFC ISIS Neutron and Muon Source, Rutherford Appleton Laboratory, UK.[26] Polaris is a high intensity, medium resolution powder diffractometer with five fixed angle detector banks covering a wide range of scattering angles between 6.7° and 167.4° 2θ. The Polaris instrument routinely achieves an accessible Q_{max} of 40 Å^{-1}, with 50 Å^{-1} being achievable with suitable samples, and for this reason, it is commonly used for total scattering experiments.

The samples were ground to ensure a fine powder, and 3 g of the air-heated sample and 5 g of the reduced–oxidized sample were separately loaded into 8 mm vanadium cans. The filled vanadium cans were then affixed onto an automatic sample changer and placed into the Polaris detector tank before the tank was evacuated. Data were collected under vacuum in eight 300 μAmps (~1 h) scans. Raw data were processed using MantidPlot.[27]

Total scattering data reduction and processing to generate the pair distribution function was performed using GudrunN[28] using all five banks of data from Polaris from 8 × ~1 h data collections. A Q_{max} of 33.5 Å^{-1} was found to be the highest usable data due to the poorly crystalline nature of the sample fired in air; for consistency, the reduced–oxidized sample was also processed using a Q_{max} of 33.5 Å^{-1}.

C. X-ray total scattering

X-ray total scattering data were acquired on the I15-1 XPDF beamline at the Diamond Light Source, Rutherford Appleton Laboratory, UK.[29] Small volumes of the sample were loaded into 0.1 mm quartz capillaries with a 0.01 mm wall thickness before being manually loaded into the beamline and aligned using a motorized sample stage. Data were collected using a 2D Perkin Elmer detector, with raw diffraction data processed into 1D diffraction patterns automatically using the DAWN (Data Analysis WorkbeNch) software at the Diamond Light Source.[30] GudrunX was used for total scattering data reduction and processing to obtain the X-PDF patterns for the studied samples.[28]

D. RMC Analysis

RMCProfile was used to analyze the PDFs using big box models.[31] The RMC starting models for both samples discussed in this

paper were generated on the ideal fluorite structure with composition $Ce_{0.75}Zr_{0.25}O_2$ based on general agreement from the neutron Bragg refinements. $12 \times 12 \times 12$ supercells with an edge length of ~64 Å and a diameter of ~111 Å based on the Bragg refined lattice parameters were chosen as a suitable box size. Atom to atom minimum distance constraints were included with values based on the experimentally observed PDFs: 1.95 Å for M–O distances and 3.30 Å for M–M distances. Additional oxygen-like vacancies were included in the final model for the reduced–reoxidized sample, which was driven primarily by unrealistic atomic migrations toward the unoccupied interstitial site (4b, 0.5, 0.5, 0.5, and $m\overline{3}m$) indicated in early RMCProfile models of the system. The inclusion of oxygen-like vacancy sites enabled oxygen atoms to swap between the oxide occupied 8c sites and the interstitial 4b sites. In both models, any iteration of the RMC random move had a probability of swapping a Ce and Zr of 0.2; for the reduced–reoxidized sample, an additional atom swap between oxygen and oxygen-like vacancies had a probability of 0.1; and all other RMCProfile iterations resulted in an atomic move. RMCProfile version 6.7.8 lacks a sufficient crystallite size function, so the crystallite size dampening envelope function from PDFgui was employed and inverted to enhance the raw data. This correction was applied to the $G(r)$ data prior to use with the RMC model.

To describe the local ordering of Ce and Zr in the large box RMC models, analysis was carried out using the Clapp configurations[25] and the quantification described by Owen *et al.*[24] Each Ce/Zr atom is considered in turn, and the arrangement of the 12 nearest neighbors in the fcc structure is characterized according to the numbering system described by Clapp.[25] The occupation of each local configuration is counted, and an enhancement factor is calculated. The enhancement factor provides a measure of the number of standard deviations the observed number of configurations is away from the expected number of configurations predicted for a random distribution of atoms in the system. The Clapp configurations shown in this work are reported as the mean enhancement of 100 RMCProfile runs in order to eliminate spurious configurations. This analysis was afforded by the exclusion of the oxide ions, considering only the cation lattice, which is in an fcc arrangement in the $Ce_{0.75}Zr_{0.25}O_2$ materials studied.

E. Other characterization

Raman spectroscopy data were collected via the Warwick Spectroscopy Research Technology Platform on a Renishaw inVia Raman microscope equipped with a 514 nm DPSS laser.

Laboratory powder x-ray diffraction data were collected via the Warwick x-ray Diffraction Research Technology Platform using a Panalytical X-Pert Pro equipped with a Cu $K\alpha_1$ focusing Johansson monochromator on the incident beam. The average data collection was between $10°$ and $120°$ 2θ over a 12 h (overnight) scan duration.

Temperature programmed reduction (TPR) was measured by the thermal conductivity of 10% H_2 in N_2 at a flow rate of 30 ml min^{-1} before and after contact with a 0.05–0.10 g sample as a function of temperature. A trap after the sample was used to absorb the water created by H_2 oxidation. The temperature was increased linearly as a function of time. In order to quantify accurately the hydrogen consumption, a known quantity (1 ml) of N_2 was injected into the H_2/N_2 gas stream before the experiment began to create

a calibration peak. The quantification of H_2 consumption was carried out by the integration of the TPR profile as a function of time, and the results are presented as the amount of H atoms oxidized per gram of sample, mmol(H) g^{-1}, which can be related to the fraction of cerium atoms reduced. The error is estimated to be ±5% for the total H_2 consumption in these measurements. Temperature programmed oxidation after the reduction of the samples showed that reoxidation readily takes place around 200 °C.

III. RESULTS AND DISCUSSION

A. Air-heated $Ce_{0.75}Zr_{0.25}O_2$

Based on the existing phase diagrams of cerium–zirconium oxides $Ce_{1-x}Zr_xO_2$, the x = 0.25 composition is expected to adopt the cubic $Fm\overline{3}m$ space group.[2] Laboratory x-ray powder diffraction was used to confirm that this was the case for our air-heated sample and that no phase segregation or crystalline impurities were present. A Rietveld refinement of the $Fm\overline{3}m$ model is shown in Figs. 1(a) and 1(b), and it shows a satisfactory match to the observed x-ray and neutron diffraction data (wR = 2.37%), and the refined parameters of this fit are shown in Table I. Oxygen site occupancy was refined and found not to deviate from the ideal stoichiometry; hence, it was fixed at 1. A broad feature was observed in the neutron diffraction data at ~2.2 Å, which would match the expected position for the forbidden 210 reflection. While the most intense Bragg reflection from the vanadium metal sample is also expected at around this d-spacing value, a small peak is visible above the background at 2.15 Å, confirming that the broad feature observed at ~2.2 Å is not this. As a result of this observation, we suggest that some order resembling the tetragonal $P4_2/nmc$ space group, usually observed in the 50:50 composition or Zr rich compositions for cerium–zirconium oxides, may be present. The lower symmetry of the tetragonal $P4_2/nmc$ space group allows for two key differences in the atomic structure compared to the $Fm\overline{3}m$ model. The first is an independent c lattice parameter, although here the observed diffraction is relatively broad, and no reflection splitting was observed, showing that the bulk average structure remains in a cubic-like arrangement. The second most important key difference afforded by the lower symmetry of the $P4_2/nmc$ space group is the variable z coordinate of the oxygen site that allows it to sit slightly off the idealized cubic site, leading to two marginally different M–O bond distances (2.29 and 2.34 Å for the $Ce_{0.75}Zr_{0.25}O_2$ sample discussed here). This gives some degree of asymmetry for the oxygen atoms, which is forbidden in the cubic space group. Cerium zirconium oxide materials with nominally cubic lattice arrangements with oxygen z coordinate displacement are also known as the pseudo-cubic phase or the $t''\text{-}Ce_{1-x}Zr_xO_2$ phase.[32]

Figures 1(c) and 1(d) show the observed x-ray and neutron data and the Rietveld calculated $P4_2/nmc$ fits of the $Ce_{0.75}Zr_{0.25}O_2$ material fired in air at 800 °C, and the refined parameters are shown in Table II. The model matches the observed data well with a wR value of 2.22%, which is a marginally better fit than that of the $Fm\overline{3}m$ structure. The visual fit across all banks is also slightly better for the $P4_2/nmc$ description, and although this may correlate with the expected outcome when adding additional parameters to any model, the analysis of total scattering described below and the diffraction from the second sample support the view that this tetragonal symmetry is the best description of the sample. It can be seen that the
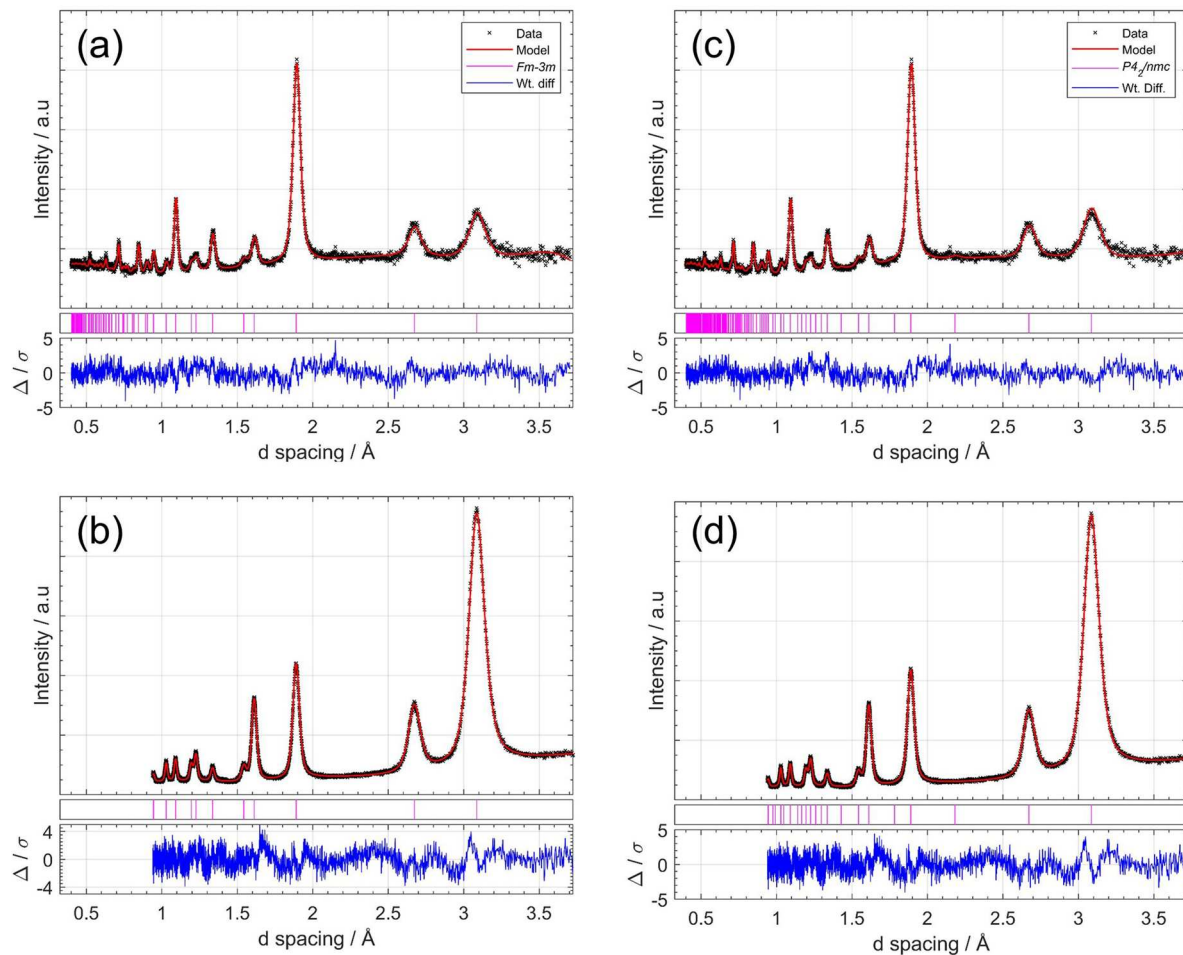
FIG. 1. Rietveld refinement of the crystal structure of $Ce_{0.75}Zr_{0.25}O_2$ heated in air at 800 °C refined simultaneously against five banks of powder neutron diffraction (Polaris) and laboratory x-ray data (Cu Kα1): (a) $Fm\bar{3}m$ model neutron data (Polaris Bank 3), (b) $Fm\bar{3}m$ model x-ray data, (c) $P4_2/nmc$ model neutron data (Polaris Bank 3), and (d) $P4_2/nmc$ model x-ray data.

tetragonal distortion of the unit cell is small, with an a/c ratio close to the ideal cubic value of 0.7071, so we refer to this model as the "pseudo-cubic model," consistent with the t″ ceria zirconia phase in the literature, noting that it maintains the extra degree of freedom in the oxide-anion position.

Figure 2 shows the fit of the pseudo-cubic model to the neutron pair distribution function using a single unit cell and the atom sites derived from the crystallographic constraints. The refined

parameters are available in Table S1. This shows a good match to the long-range order, but the short-medium range order shows a significant mismatch in the <10 Å region, highlighting that the local structure of this material cannot be described by the long-range average structure. To better understand the local structure, reverse Monte Carlo modeling was undertaken using the neutron total

TABLE I. Refined parameters for $Ce_{0.75}Zr_{0.25}O_2$ using the face centered cubic $Fm\bar{3}m$ space group, $a = 5.3458(1)$ Å. Calculated density: 7.0471 g/cm³ wR = 2.37%.

Atom	Symmetry	x	y	z	U_{iso} (Å²)	Occupancy
Ce	m3m	0	0	0	0.0080(1)	0.75
Zr	m3m	0	0	0	0.0080(1)	0.25
O	−43m	¼	¼	¼	0.0177(1)	1

TABLE II. Refined parameters for $Ce_{0.75}Zr_{0.25}O_2$ using the tetragonal $P4_2/nmc$ space group in the second origin: $a = 3.7802(6)$ Å, $c = 5.3436(16)$ Å, a/c ratio = 0.7074 (ideal cubic ratio = 0.7071). Calculated density = 6.954 g/cm³, oxygen "displacement" from cubic z coordinate = 0.0134, and wR = 2.22%.

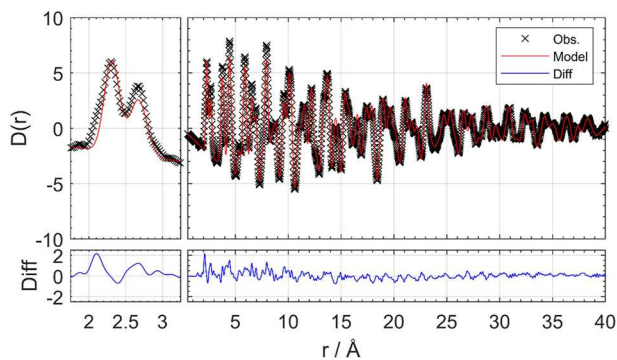| Atom	Symmetry	x	y	z	U_{iso} (Å²)	Occupancy
Ce	−4m2(z)	¼	−¼	¼	0.0045(1)	0.75
Zr	−4m2(z)	¼	−¼	¼	0.0045(1)	0.25
O	mm2(z)	¼	¼	0.4866(3)	0.0095(2)	1

FIG. 2. Neutron pair distribution function D(r) of $Ce_{0.75}Zr_{0.25}O_2$ heated in air at 800 °C and the calculated pattern from the pseudo-cubic structure. The left panel shows an expanded view of the low r region.

scattering data, with simultaneous fitting of the model against both the Bragg diffraction pattern and the PDF. The starting model used was based on the cubic structure with space group $Fm\bar{3}m$ to generate a 12 × 12 × 12 supercell (edge length = 64.175 Å) containing 20 736 atoms. The cubic model was chosen so as not to bias our conclusion of local structural distortions allowed by the average structure having a tetragonal space group. An inverse crystallite size function was applied during the fitting to correct for the r-range dampening observed using a crystallite size of ~90 nm. Figure 3 shows the final atomic configuration achieved after 1 802 176 accepted moves

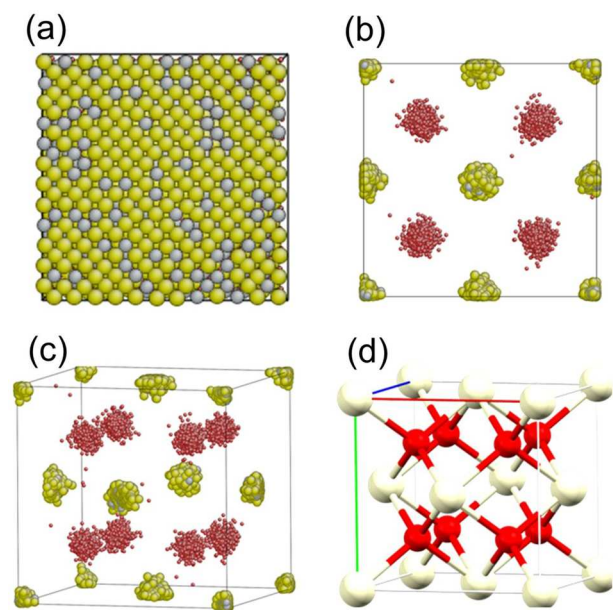**FIG. 3.** Final RMC derived atomic configuration for $Ce_{0.75}Zr_{0.25}O_2$ heated in air at 800 °C. (a) RMC generated a supercell containing 20 736 atoms. (b) Supercell collapsed into a single fluorite unit cell, viewed parallel to a single face. (c) Perspective view: yellow = cerium, gray = zirconium, and red = oxygen. (d) View of the single unit cell of the initial model: red = regular oxygen site and white = metal site.

and 23 312.77 s, while Fig. 4 shows the fits achieved to the Bragg scattering and neutron PDF.

Several approaches were used to analyze the large number of atoms present in the derived configurations of atoms. Figure 5(a) shows a histogram of atomic displacements from the initial crystallographic sites for each atom type. It is observed that the Ce appears to be marginally more displaced compared to Zr, with nearly all Zr displacements being smaller than 0.3 Å, while the Ce displacement is still evident to be 0.4 Å.

In the original $Fm\bar{3}m$ model, all four cation sites and all eight oxygen sites are equivalent; however, as the RMC model is generated with no symmetry constraints, each of these equivalent sites becomes independent, and so, for the purposes of analysis in this study, each is assigned a "Primitive Site ID" number. Primitive (P1) site IDs 1–4 are the symmetrically equivalent Ce/Zr occupied 0, 0, 0 $m3m$ site, and P1 site IDs 5–12 are the symmetrically equivalent 1/4, 1/4, 1/4, $-43m$ O occupied site of the original $Fm\bar{3}m$ structure. P1 site IDs and ideal atomic coordinates are shown in Table S2. The occupancy histograms, Fig. S1, show that, consistent with the average structure, all four cation sites are approximately Ce = ~75% and Zr = ~25%, with no evidence of any cation order. Due to the model being built with full oxygen occupancy (assumed for charge balance and consistent with the Rietveld analysis), analysis of the occupancy of the eight oxygen sites was not informative in this system.

Figure 5(b) shows the histograms of the nearest cation neighbor species and distance for both cation types. The cation species and the
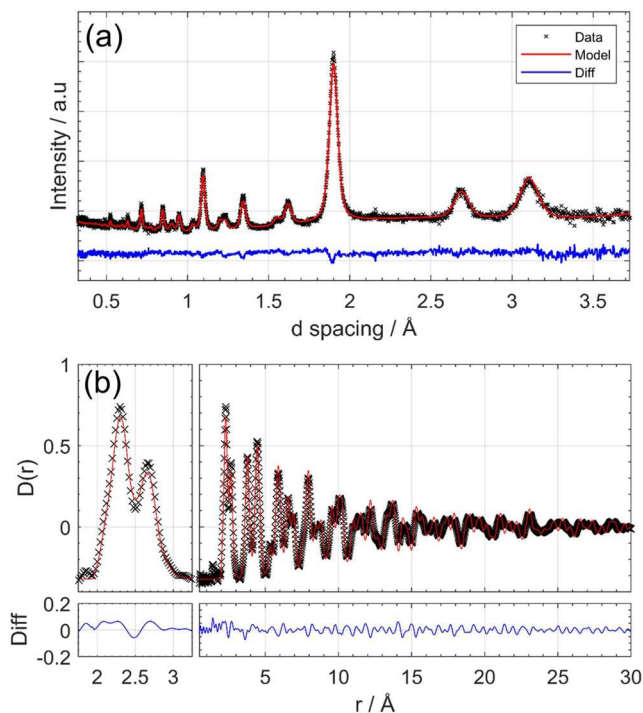

FIG. 4. Datasets and calculated patterns from the RMC generated 12 × 12 × 12 supercell for the air-heated sample. (a) Powder neutron diffraction acquired on Polaris Bank 3. (b) Neutron pair distribution function, with the left panel showing the low r region.
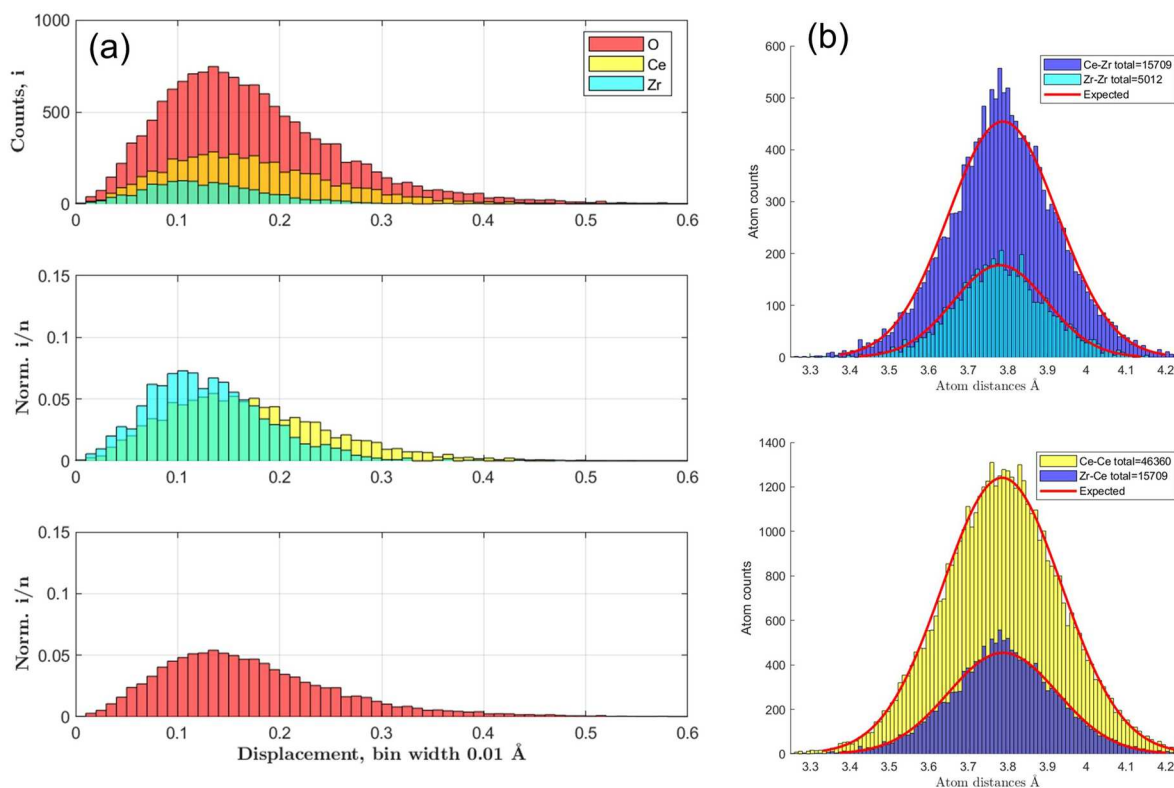
FIG. 5. (a) Histogram of atomic displacement counts by species for the air-heated sample. Counts: Total = 20 736; Ce = 5184; Zr = 1728; O = 13 824. Displacement distance is measured from the $Fm\bar{3}m$ idealized coordinate. Top: all displacements by atomic species. Middle: cation (Ce, Zr) site displacements by atomic species. Bottom: anion (O) site displacements by atomic species. (b) Histogram of the nearest neighbor cation count and distance by species, for the same sample. The red line shows the expected intensity profile for a single distribution, which is compositionally defined. Top: Zr–Zr and Zr–Ce. Bottom: Ce–Ce and Ce–Zr.

magnitude of interatomic distances between each of these pairings match the statistically expected values for a solid solution. Combined with the atom site occupancy information discussed above, this indicates that, on average, there is no specific ordering of cations on each symmetrically equivalent site and no clustering of cations across nano-sized regions of the model. In summary, this paints the picture that this model fits the classical description of a solid-solution material with no local ordering of cations present.

To further test this idea, Fig. 6 shows a representation of the relative local structure of the cerium and zirconium fluorite lattice undertaken via Clapp configuration analysis.[25] This is possible because, by ignoring the oxygen atoms, the cation sublattice can be visualized as though it were a binary alloy. In an fcc binary system, there are 12 atoms in the nearest cation neighbor shell, and with the inclusion of the central atom, there are a total of 144 possible symmetrically unique arrangements for these 13 atoms. Each of these so-called Clapp configurations[25] is labeled with a positive or negative integer based on whether the shell consists of primarily "like" or "unlike" atoms, respectively, relative to the central atom. Labels close to 0 represent configurations with large numbers of like (positive) or unlike (negative) atomic neighbors. For example, the Clapp configuration C1 represents a case where all 12 nearest neighbors are the same species as the central atom, and configuration
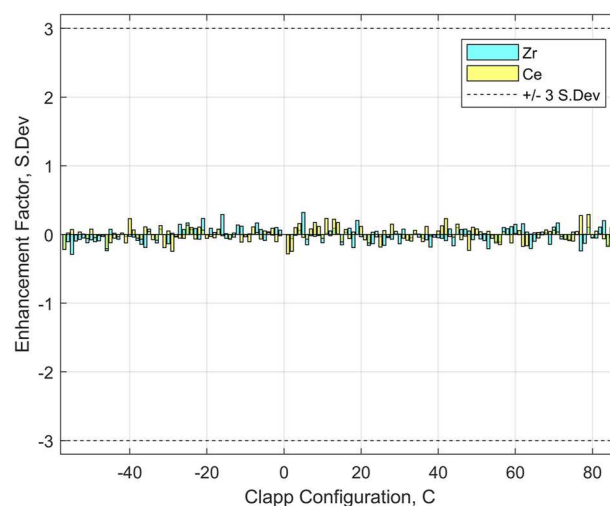

FIG. 6. Clapp configurations determined from the 12 × 12 × 12 RMC-refined supercell for the air-heated sample, with configuration counts normalized to the statistical probability of occurrence and plotted in predicted standard deviations away from the statistical probability of occurrence.

$C-1$ is the inverse situation where all 12 neighbors are not the same as the central atom. (For clarity, there is no configuration labeled 0.) The abundance of each Clapp configuration in the RMC model was determined, and an enhancement factor was calculated.[24] The enhancement factor (β) provides a measure of the number of standard deviations (σ) the calculated abundance of a particular configuration (x) is away from the expected abundance (μ) with $\beta = \frac{x-\mu}{\sigma}$ within a particular configurational setup. These enhancement factors, as plotted in Fig. 6, show that for this material, all 144 possible configurations (for the fcc structure) match closely to the stoichiometrically predicted probability of occurrence (EF = 0 baseline), as is expected in the case of a statistically homogeneous solid solution with a compositionally average local structure.

B. Reduced–oxidized Ce$_{0.75}$Zr$_{0.25}$O$_2$

The data analysis of the reduced–oxidized sample was performed using the same approach as for the air-heated sample, but

since greater structural deviation was detected from the ideal model (see below), an additional dataset was included to aid the RMC analysis, namely, a PDF derived from x-ray scattering. As with the air-heated sample, the Bragg diffraction pattern, Fig. 7, is consistent with a single-phase material with cubic symmetry. No peak splitting is observed. However, due to the relatively sharper reflection profile after the additional heated treatment, the FCC forbidden 210 reflection is clearly observed in the weighted difference plot of Fig. 7(d), seen as a broad feature at 2.2 Å, slightly overlapping with the sharp vanadium reflection at 2.15 Å. As described for the air-heated sample above, this reflection can be assigned as the 210 reflection of the tetragonal $P4_2/nmc$ space group, as expected for the pseudo-cubic t$''$ phase of Ce$_{1-x}$Zr$_x$O$_2$ when x $\approx$ 0.5. As with the air-heated sample discussed above, the $Fm\bar{3}m$ model fit (wR 3.68%) gave a slightly worse fit to the observed data than the $P4_2/nmc$ model fit (wR 3.44%), Fig. 7 and Tables III and IV. Oxygen site occupancy was refined and, as with the other material, was found not to deviate from the ideal stoichiometry and, hence, was fixed at 1.
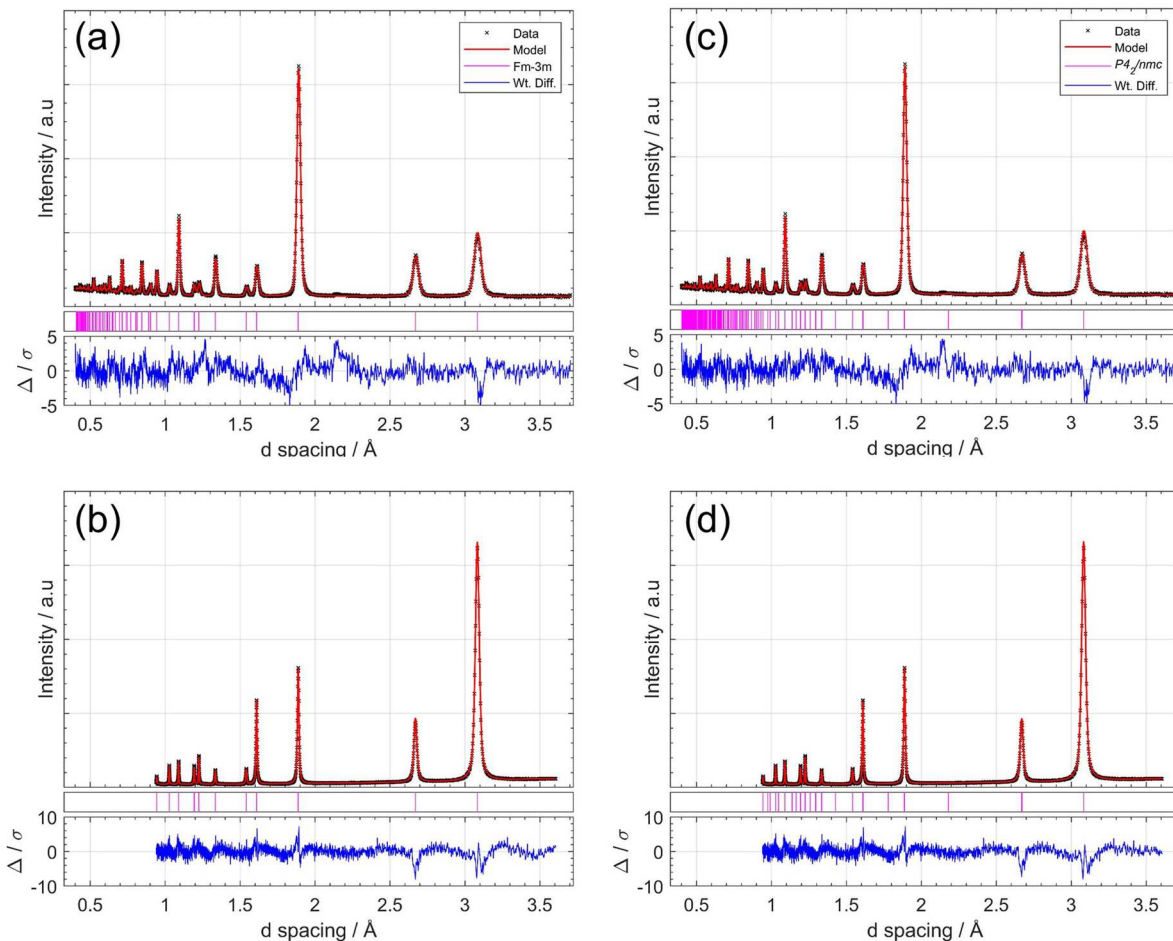

FIG. 7. Rietveld refinement of the crystal structure of Ce$_{0.75}$Zr$_{0.25}$O$_2$ after reduction–reoxidation refined simultaneously using five banks of powder neutron diffraction data (Polaris) and laboratory x-ray data (Cu Kα1): (a) $Fm\bar{3}m$ model neutron data (Polaris Bank 3), (b) $Fm\bar{3}m$ model x-ray data, (c) $P4_2/nmc$ model neutron data (Polaris Bank 3), and (d) $P4_2/nmc$ model X-ray data.

TABLE III. Refined parameters for $Ce_{0.75}Zr_{0.25}O_2$ using the face centered cubic $Fm\bar{3}m$ space group, a = 5.33935(5) Å. Calculated density = 6.977 g/cm^3; wR = 3.68%.

Atom	Symmetry	x	y	z	U_{iso} (Å^2)	Occupancy
Ce	m3m	0	0	0	0.00442(5)	0.75
Zr	m3m	0	0	0	0.00442(5)	0.25
O	−43m	1/4	1/4	1/4	0.01062(5)	1

TABLE IV. Refined parameters for $Ce_{0.75}Zr_{0.25}O_2$ using the tetragonal $P4_2/nmc$ space group in the second origin, a = 3.7743(1) Å, c = 5.3422(3) Å, and a/c ratio = 0.7065 (ideal cubic ratio = 0.7071). Calculated density = 6.977 g/cm^3, oxygen "displacement" from cubic z coordinate = 0.009 11, and wR = 3.44%.

Atom	Symmetry	x	y	z	U_{iso} (Å^2)	Occupancy
Ce	−4m2(z)	1/4	−1/4	1/4	0.00430(5)	0.75
Zr	−4m2(z)	1/4	−1/4	1/4	0.00430(5)	0.25
O	mm2(z)	1/4	1/4	0.4909(1)	0.00958(6)	1

Figure 8 shows a fit to the neutron PDF using the crystallographically constrained pseudo-cubic model. Notably, the average model fits the short-medium range better, with no clear mismatch in the <10 Å region observed for the air-heated sample. However, some deviation between the average and short range structures was still observed, although not to the same extent as for the air-heated sample. The reduced–oxidized sample was also investigated using an initial 12 × 12 × 12 fluorite supercell configuration; however, in the initial investigation, it became apparent that additional atomic sites were required to better fit the data since the movement of atoms from their original site to an interstitial site in the $Fm\bar{3}m$ structure (4b, 0.5, 0.5, 0.5, $m\bar{3}m$) was observed. This represents a Frenkel-type anion defect, with distances from this site to the neighboring oxide and cations matching those of O–O and O–Ce/Zr, respectively. To accommodate this and probe the amount of interstitial oxygen present, an oxygen-like vacancy site was introduced on the 4b site with an initial site occupancy of ~10%, representing 5% of the total O content. During RMC refinement, atom-site swaps were allowed between these oxygen-like vacancies and oxygen atoms, thus keeping the overall stoichiometry of the supercell balanced while probing interstitial oxygen content. Figure 9 shows the final refined RMC configurations as collapsed unit cells alongside the classical starting models used for the reduced–oxidized $Ce_{0.75}Zr_{0.25}O_2$ material, while Fig. 10 shows the RMCProfile obtained fits achieved to the neutron and x-ray PDFs of the final atomic configuration achieved after 429 434 accepted moves and 22 961.18 s.

Figure 11(a) shows a histogram of atomic displacement for the final model, which shows several key differences compared to the model for the air-heated sample discussed above. Zr appears to be more uniform in displacement with a slightly lower average displacement, while Ce appears to have a bimodal displacement profile.

The cation site occupancy for the model shows no average structure preference based symmetrically equivalent sites, confirming that the model has not formed any long-range features that were not observed in the Bragg diffraction and that the expected ratio
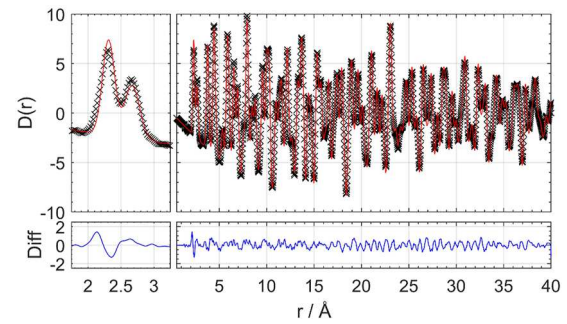

FIG. 8. Neutron pair distribution function D(r) and calculated patterns of $Ce_{0.75}Zr_{0.25}O_2$ after reduction–reoxidation in the pseudo-cubic structure. The left panel shows an expanded view of the low r region.

of 75% Ce and 25% Zr is approximately maintained across each cation site within each unit cell across the supercell model (Fig. S2 and Table S3). The overall oxygen occupancy of the interstitial sites equated to 2.105% of the overall oxygen present, giving the system studied the formula of $Ce_{0.75}Zr_{0.25}O_{1.958}(O_i)_{0.042}$, where (O_i) is the Frenkel-type interstitial oxygen described above. The associated oxygen vacancies are distributed over all possible oxide sites, with no evidence of preferred deficiency of particular sites (Fig. S3). Interstitial oxygen sites in ceria based materials have been mentioned in the literature previously. Luo et al. conducted a Raman spectroscopy and neutron total scattering study investigating surface oxygen defects in CeO_2, finding between 2.8% and 4% in bulk CeO_2 nano-cubes with
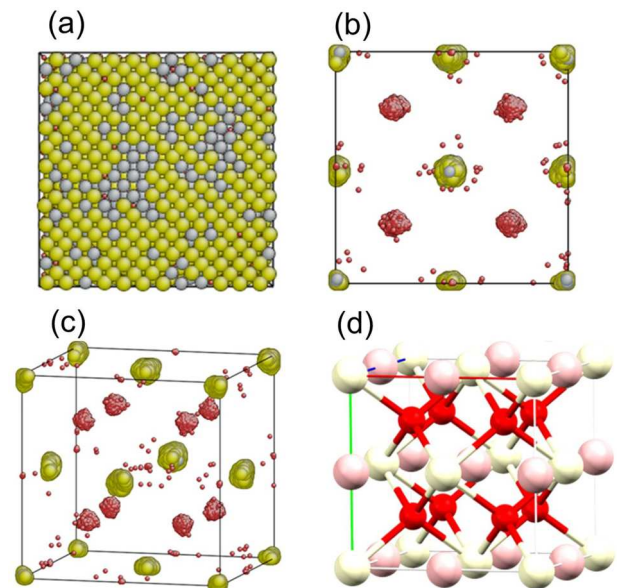

FIG. 9. Final RMC derived atomic configuration for $Ce_{0.75}Zr_{0.25}O_2$ after reduction–reoxidation at 800 °C. (a) RMC generated supercell containing 20 736 atoms. (b) Supercell collapsed into a single fluorite unit cell, viewed parallel to a single face. (c) Perspective view: yellow = cerium, gray = zirconium, and red = oxygen. (d) View of the single unit cell of the initial model: red = regular oxygen site, white = metal site, and pink = interstitial oxide site.
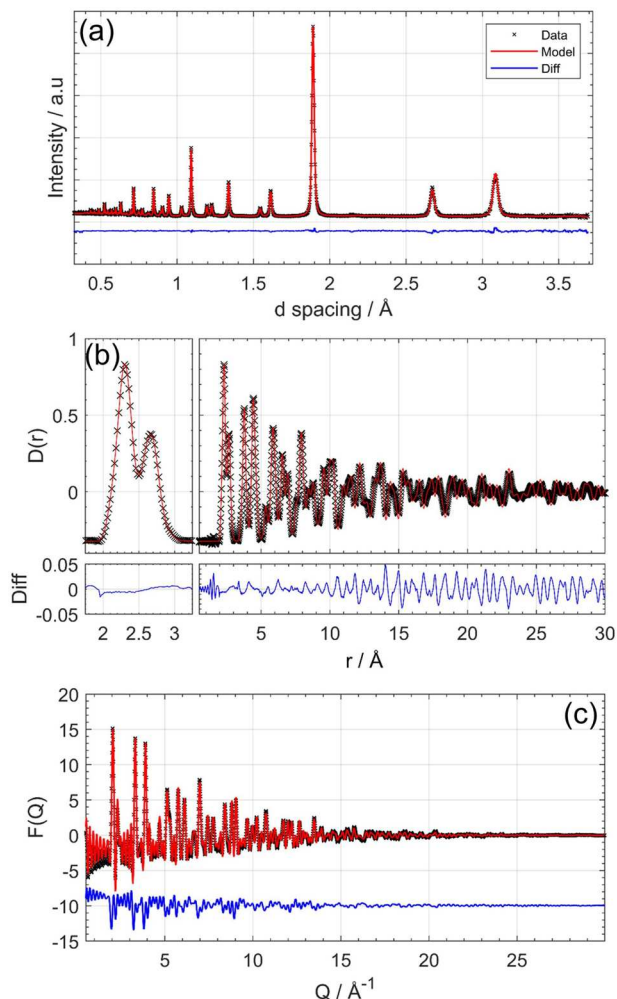
19 January 2024 15:49:14

FIG. 10. Datasets and calculated patterns from the RMC generated $12 \times 12 \times 12$ supercell for the reduced–oxidized sample. (a) Powder neutron diffraction acquired on Polaris Bank 3, (b) neutron pair distribution function full fitted region extended to 30 Å, with the left panel showing the low r region, and (c) x-ray $F(Q)$ data acquired from I15-1.

additional oxygen deficiency and Frenkel-type defects in a surface nano-rod phase of Ce_3O_{5+x}. These Frenkel-type oxygen defects were further related to the observed oxygen storage capacity properties.[33] This level of Frenkel-type defects is very similar to those observed here in the reduced–oxidized material. A study by Mamontov and Egami used neutron diffraction, electron paramagnetic resonance, and temperature programmed reduction to study oxygen vacancies and interstitial oxygen defects in CeO_2 and $Ce_{0.7}Zr_{0.3}O_2$ and concluded that the presence of zirconium showed a stabilizing influence on these defects via the reduction of Ce^{4+} to Ce^{3+}, giving increased resistance to thermal sintering.[34] This work claimed that interstitial oxygen defects are the source of cerium–zirconium oxides oxygen storage capacity properties and that further stabilization of these defects would further improve the thermal resistance of these supports.

Figure 11(b) shows a histogram of the cation–cation distances. Unlike with the air-heated sample, the ratio of nearest neighbors observed for this reduced–oxidized sample is not equivalent to the stoichiometry defined ratios and there is a distinct preference shown for same species neighbors, which is statistically more significant for the Zr–Zr neighboring. This neighboring preference strongly implies the existence of same-species clustering within the structure. These domains only occur over short length scales, a few nanometers, since Bragg diffraction provides no evidence for long-range phase separation. Inhomogeneous nano-domains have previously been observed in ceria-zirconia materials by Mamontov *et al.,* who undertook a pulsed neutron scattering study on various $Ce_{0.5}Zr_{0.5}O_2$ samples and found that their samples were better described as nano-regions of $Ce_{0.4}Zr_{0.6}O_2$ in a matrix of $Ce_{0.7}Zr_{0.3}O_2$.[23] While the composition clearly differs, the observation of Zr rich nano-domains is in agreement with the results indicated by this RMC study, even in a cerium-rich phase.

The preference for local clustering of like cations is confirmed by the Clapp configuration analysis, Fig. 12. Unlike the solid solution found for the air-heated material described above, the reduced–oxidized material shows a significant number of enhanced Clapp configurations (i.e., different local environments) with occurrences well above 3 standard deviations, representing a 99.7% level of confidence against random chance. In particular, both Ce and Zr centered configurations showed statistically significant enhancements of $C1$ and $C2$, which contain 12 and 11 like nearest neighbors, respectively, suggesting that both Ce and Zr have increased like–like local atomic correlations; however, the statistical importance of these enhancements differs due to the different amounts of Ce and Zr in this system.

The Ce centered configurations $C1$ and $C2$ are highlighted because Ce makes up 75% of the cations in the material, meaning that we would expect a significant number of occurrences with a large predicted standard deviation. This results in the observed enhancement in Ce centered $C1$ and $C2$ configurations being particularly significant and is visually highlighted when considering the magnitude of the standard deviation error bars for Ce configurations $C1$ and $C2$, as shown in Fig. 12(a).

The Zr shows an increase in the positive Clapp configurations (in particular, $C1$–$C57$) and a decrease in the negative configurations ($C-1$ to $C-8$). Low numbered positive Clapp configurations have a higher local concentration of like-atoms, suggesting that Zr atoms are preferentially found in local environments with increased Zr neighbors. This is in agreement with the observation from the Ce, as the increase in Ce–Ce correlations will result in a decrease in Ce–Zr and a comparative increase in Zr–Zr. It should be noted that as the concentration of Zr is low in the material, the predicted standard deviation in the number of configurations with high local concentrations of Zr will be exceptionally small. Consequently, as a multiple of standard deviations, the increase in the low positive Clapp configurations (e.g., $C1$–$C16$) will appear very large, even for a small increase in these configurations; for instance, due to the stoichiometry, a single occurrence of Zr fully surrounded by Zr cations would produce an enhancement factor of 98 due to the extreme statistically unlikelihood of occurrence; however, with such few observed occurrences, the statistical significance of the observed Zr centered $C1$ configuration is not robust, as highlighted by the magnitude of the error bars shown in Fig. 12(a). For the same reason, the Ce centered
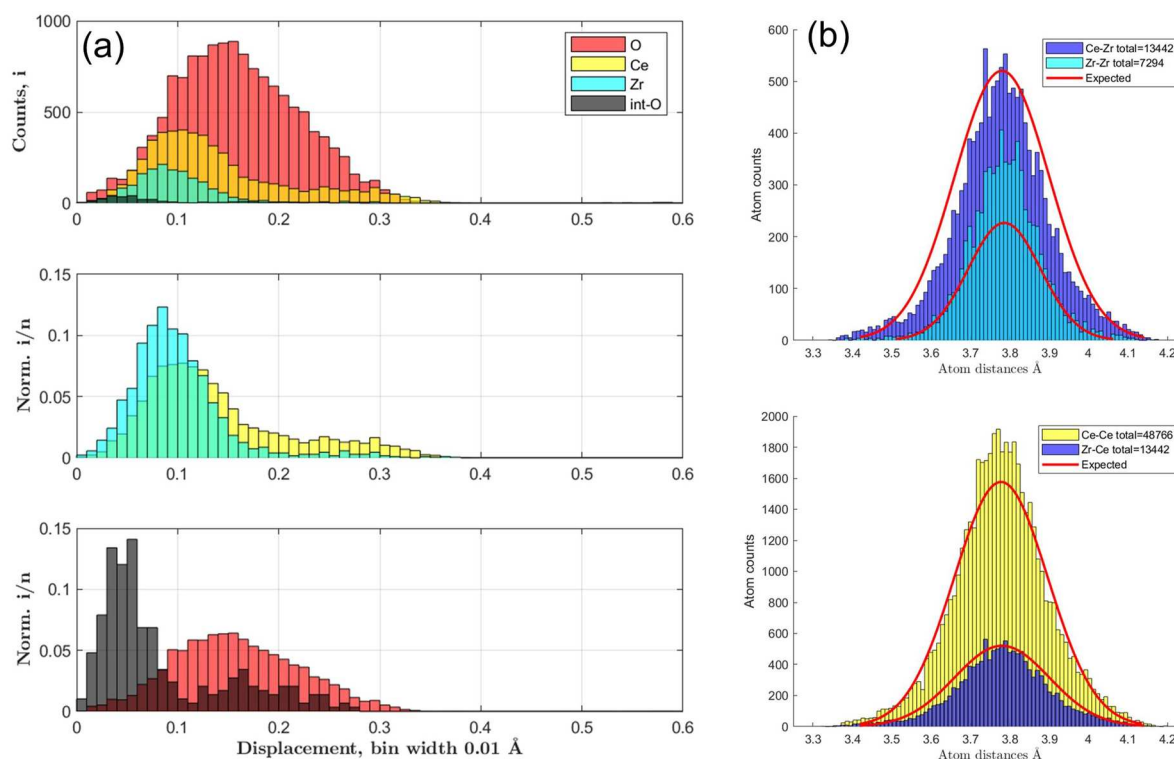
19 January 2024 15:49:14

FIG. 11. (a) Histogram of atomic displacement counts by species for the reduced–oxidized sample. Counts: Total = 20 736; Ce = 5184; Zr = 1728; O = 13 824. Displacement distance measured from the $Fm\bar{3}m$ idealized coordinate. Top: all displacements by atomic species. Middle: cation (Ce, Zr) site displacements by atomic species. Bottom: anion (O) site displacements by atomic species. (b) Histogram of the nearest neighbor cation count and distance by species, for the same sample. The red line shows the expected intensity profile for a single distribution, which is compositionally defined. Top: Zr–Zr and Zr–Ce. Bottom: Ce–Ce and Ce–Zr.

$C-1$ configuration also suffers from statistical unreliability also captured in Fig. 12(a).

By probing the configurations with good statistical reliability, the conclusion of a statistically significant increase in Ce–Ce nearest neighbor correlations and a significant decrease in Ce–Zr nearest neighbor correlations can be drawn, strongly indicating the presence of cation-rich nano-domains.

C. Additional characterization

The two materials were studied by Raman spectroscopy, as shown in Fig. 13(a). The primary Raman band of both spectra observed at 475 cm^{-1} is associated with the highly symmetric M–O bond distances of the $Fm\bar{3}m$ structure, and this band is broadened compared to that expected for the CeO$_2$ structure,[10,11] showing that a degree of disorder in the M–O vibrational states is observed. Additionally, two moderate features are noted at ~300 and ~600 cm^{-1}, matching the major two features of the t-ZrO$_2$ ($P4_2/nmc$) structure. This supports the combined x-ray and neutron diffraction conclusions that the structure present cannot be fully explained in the $Fm\bar{3}m$ space group due to the cubic symmetry constraints but can be described by a cubic unit cell with a distorted oxygen lattice, also referred to as the pseudo-cubic t″ structure more

recognized in Ce$_{0.5}$Zr$_{0.5}$O$_2$ compositions.[32] There are notable key differences between the two materials; in particular, the sample after reduction–oxidation has two additional minor bands at ~420 and ~575 cm^{-1}. These additional bands do not match any band expected in the CeO$_2$ or t-ZrO$_2$ structures. Andriopoulou *et al.* identified a similar broad band at ~630 cm^{-1} during the reduction and oxidation of Ce$_{0.8}$Zr$_{0.2}$O$_2$ and accredited the band to Frenkel-type defected oxygen occupying interstitial sites,[35] so this assignment would be consistent with the conclusions of the RMC model generated for the reduced–oxidized material. The Raman band at ~425 cm^{-1} remains unassigned at this stage; however, one hypothesis for this band could be nano-domain phase segregation giving rise to a minority of more CeO$_2$-like M–O vibrations, which would be expected to be redshifted from the bulk solid state band, which itself appears to be blueshifted compared to the air-heated material.

Temperature programmed reduction (TPR) profiles are shown in Fig. 13(b), where both samples were heated under a constant flow of 5% H$_2$ in N$_2$ with hydrogen uptake measured. Both samples were measured twice with an intermediate mild oxidation applied between each TPR to gauge stability, and these are referred to as TPR1 and TPR2. The profiles clearly show some distinctive differences between the two samples, with the air-heated sample showing
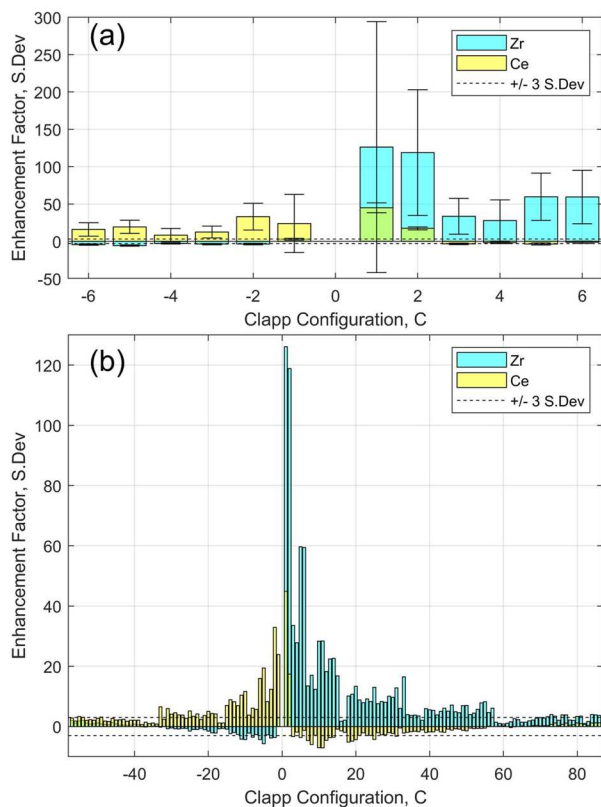
FIG. 12. Clapp configurations determined from the $12 \times 12 \times 12$ RMC-refined supercell for the reduced–oxidized sample, where configuration counts have been normalized to the statistical probability of occurrence and are plotted in predicted standard deviations away from the statistical probability of occurrence. (a) Configurations and observed standard deviations of Clapp configurations $C-6$ to $C6$. (b) Full range of Clapp configurations observed.

FIG. 13. (a) Raman spectra of $Ce_{0.75}Zr_{0.25}O_2$ materials obtained using a 514 nm CO laser. The black dotted lines indicate CeO_2- or ZrO_2-like bands present in both samples. The red dotted lines indicate bands only observed in the reduced–oxidized sample. (b) Temperature programmed reduction profiles of both samples measured under 10% H_2–N_2. Two cycles are shown, between which a mild oxidation was carried out.

H_2 uptake at slightly lower temperatures and slightly more reduction achieved overall at 2.85 (TPR1) and 2.93 (TPR2) mmol H atoms/g, indicating a Ce^{4+} to Ce^{3+} reduction of 60.8% and 62.5%, respectively. The reduced–oxidized sample showed a similar reduction between TPR1 and TPR2, which was expected as the sample has already undergone a high temperature reduction as part of its preparation; however, it showed marginally poorer H_2 uptake with 2.77 (TPR1) and 2.78 (TPR2) mmol H/g, indicating 59.0% and 59.2% Ce^{4+} to Ce^{3+} reduction, respectively. Crystallite size differences could be partially responsible for the difference in redox properties between the two samples, as smaller crystallites are often accredited with more surface area and, thus, active cerium atoms; however, various studies have found that crystallite size itself is not the defining factor but rather the removal of oxygen defects that also accompanies sintering.[34] The difference in TPR results may also be ascribed to the nano-domain phase segregation present in the reduced–oxidized sample since homogeneous ceria-zirconia solid solutions are expected to have a better performance, and the presence of interstitial oxygen ions, even at a low level, could conceivably alter the oxygen transport properties of the materials.
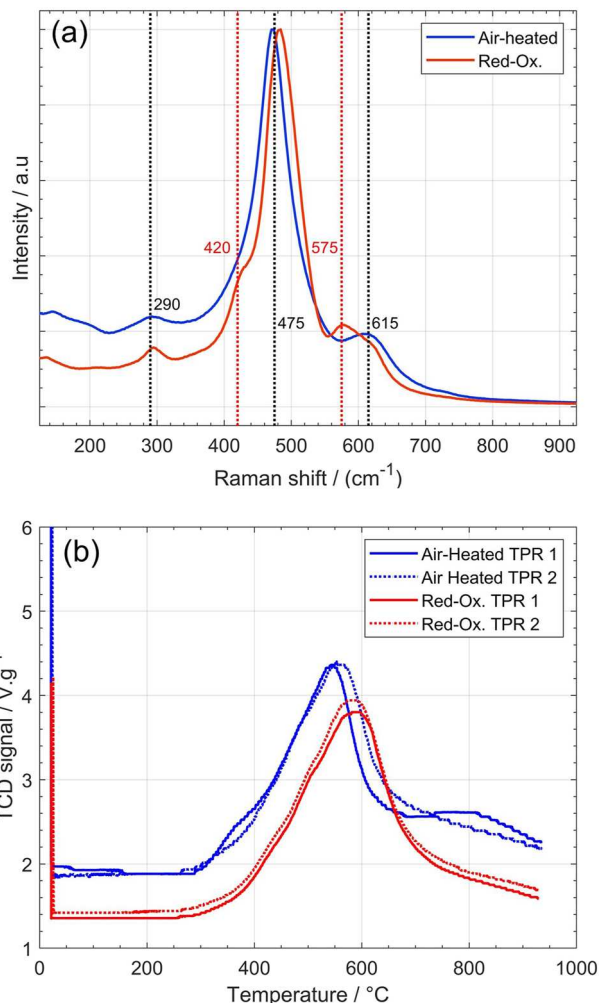
IV. CONCLUSIONS

An in-depth analysis of total scattering from a material in the well-studied ternary oxide system of ceria-zirconia has yielded new insights into structural chemistry that are not visible using conventional laboratory diffraction and spectroscopic analysis. When subjected to a relatively mild in-air heat treatment, $Ce_{0.75}Zr_{0.25}O_2$ shows all the characteristics of a homogeneous solid solution with statistical distribution of the cations over a cubic fluorite-like structure. Small deviations from the average structure are driven by the differences in coordination preference for Zr compared to Ce. In contrast, after a reduction–reoxidation process, similar to the one that would be used to screen redox properties, and mimicking redox cycling that might take place in practical applications,

19 January 2024 15:49:14

the structure of the material changes notably. In particular, the presence of Frenkel oxide-ion defects is generated by the redox cycle, along with a non-statistical distribution of cations, such that like next-nearest neighbors are preferred. This nanoscale "ordering" into zirconium-rich domains in cerium-rich oxide is not something that has previously been observed, and this might correspond to the onset of phase separation. This phase separation is known from the literature to occur more readily under oxidative conditions and for more Zr-rich phases, but evidently, cation rearrangement is brought about under redox conditions even for Ce-rich compositions. Our study illustrates how an analysis of total scattering provides a new level of detail concerning the structures of the well-studied ternary oxides, but the challenge in future work will be to measure and interpret *operando* time-resolved total scattering in order to follow the evolution of nanostructures under operating conditions.

SUPPLEMENTARY MATERIAL

The supplementary material contains additional analysis of the refined RMC models.

DEDICATION

Dedicated to Professor Sir Tony Cheetham on the occasion of his 75th birthday.

ACKNOWLEDGMENTS

AUTHOR DECLARATIONS

Conflict of Interest

The authors have no conflicts to disclose.

Author Contributions

A.S. designed and performed the experiments, analyzed the data, and prepared the first draft of the manuscript. H.Y.P. assisted with the neutron data collection, supervised the data analysis, and helped with revising the manuscript. L.R.O. assisted with the Clapp configuration analysis. J.M.F. measured TPR and heat treated the samples used in this study, A.K. and D.T. assisted with interpretation of the structural models. R.I.W. supervised the work and oversaw preparation and revision of the manuscript. All authors have reviewed and approved the manuscript.

Aron Summer: Formal analysis (equal); Investigation (equal); Methodology (equal); Writing – original draft (equal); Writing – review & editing (equal). **Helen Y. Playford**: Conceptualization (equal); Formal analysis (equal); Methodology (equal); Software (lead); Supervision (equal); Writing – review & editing (equal). **Lewis R. Owen**: Formal analysis (equal); Methodology (equal). **Janet Fisher**: Investigation (equal); Supervision (equal); Writing – review & editing (equal). **Amy Kolpin**: Investigation (equal). **David Thompsett**: Conceptualization (equal); Supervision (equal); Writing – review & editing (equal). **Richard I. Walton**: Conceptualization (equal); Formal analysis (equal); Funding acquisition (lead); Project administration (lead); Resources (lead); Supervision (equal); Writing – review & editing (equal).

DATA AVAILABILITY

REFERENCES

[1] R. Di Monte and J. Kašpar, Catal. Today **100**, 27 (2005).

[2] T. Montini, M. Melchionna, M. Monai, and P. Fornasiero, Chem. Rev. **116**, 5987 (2016).

[3] G. Kim, Ind. Eng. Chem. Prod. Res. Dev. **21**, 267 (1982).

[4] R. J. Gorte and S. Zhao, Catal. Today **104**, 18 (2005).

[5] I. I. Soykal, H. Sohn, D. Singh, J. T. Miller, and U. S. Ozkan, ACS Catal. **4**, 585 (2014).

[6] Q. Wang, K. L. Yeung, and M. A. Bañares, Catal. Today **356**, 141 (2020).

[7] S. Liu, X. Wu, D. Weng, and R. Ran, J. Rare Earths **33**, 567 (2015).

[8] A. Le Gal, S. Abanades, N. Bion, T. Le Mercier, and V. Harlé, Energy Fuels **27**, 6068 (2013).

[9] R. Schmitt, A. Nenning, O. Kraynis, R. Korobko, A. I. Frenkel, I. Lubomirsky, S. M. Haile, and J. L. M. Rupp, Chem. Soc. Rev. **49**, 554 (2020).

[10] P. Li, X. Chen, Y. Li, and J. W. Schwank, Catal. Today **327**, 90 (2019).

[11] F. Zhang, C.-H. Chen, J. C. Hanson, R. D. Robinson, I. P. Herman, and S.-W. Chan, J. Am. Ceram. Soc. **89**, 1028 (2006).

[12] R. Grau-Crespo, N. H. de Leeuw, S. Hamad, and U. V. Waghmare, Proc. R. Soc. London, Ser. A **467**, 1925 (2011).

[13] I. Gasser, M. Rybicki, and W. Wollner, Comput. Math. Appl. **67**, 1521 (2014).

[14] C. A. Young and A. L. Goodwin, J. Mater. Chem. **21**, 6464 (2011).

[15] E. Mamontov and T. Egami, J. Phys. Chem. Solids **61**, 1345 (2000).

[16] M. Coduri, M. Scavini, M. Allieta, M. Brunelli, and C. Ferrero, J. Phys.: Conf. Ser. **340**, 012056 (2012).

[17] M. Scavini, M. Coduri, M. Allieta, M. Brunelli, and C. Ferrero, Chem. Mater. **24**, 1338 (2012).

[18] R. L. McGreevy and P. Zetterström, Curr. Opin. Solid State Mater. Sci. **7**, 41 (2003).

[19] H. Y. Playford, L. R. Owen, I. Levin, and M. G. Tucker, Annu. Rev. Mater. Res. **44**, 429 (2014).

[20] A. H. Clark, H. R. Marchbank, T. I. Hyde, H. Y. Playford, M. G. Tucker, and G. Sankar, Phys. Scr. **92**, 034002 (2017).

[21] S. Hull, S. T. Norberg, I. Ahmed, S. G. Eriksson, D. Marrocchelli, and P. A. Madden, J. Solid State Chem. **182**, 2815 (2009).

19 January 2024 15:49:14

[22] W. Ji, N. Wang, Q. Li, H. Zhu, K. Lin, J. Deng, J. Chen, H. Zhang, and X. Xing, Inorg. Chem. Front. **9**, 275 (2022).

[23] E. Mamontov, R. Brezny, M. Koranne, and T. Egami, J. Phys. Chem. B **107**, 13007 (2003).

[24] L. R. Owen, H. Y. Playford, H. J. Stone, and M. G. Tucker, Acta Mater. **125**, 15 (2017).

[25] P. C. Clapp, Phys. Rev. B **4**, 255 (1971).

[26] R. I. Smith, S. Hull, M. G. Tucker, H. Y. Playford, D. J. McPhail, S. P. Waller, and S. T. Norberg, Rev. Sci. Instrum. **90**, 115101 (2019).

[27] O. Arnold, J. C. Bilheux, J. M. Borreguero, A. Buts, S. I. Campbell, L. Chapon, M. Doucet, N. Draper, R. F. Leal, M. A. Gigg, V. E. Lynch, A. Markvardsen, D. J. Mikkelson, R. L. Mikkelson, R. Miller, K. Palmen, P. Parker, G. Passos, T. G. Perring, P. F. Peterson, S. Ren, M. A. Reuter, A. T. Savici, J. W. Taylor, R. J. Taylor, R. Tolchenov, W. Zhou, and J. Zikovsky, Nucl. Instrum. Methods Phys. Res., Sect. A **764**, 156 (2014).

[28] A. K. Soper, RAL Technical Reports Report No. RAL-TR-2011-013, Science and Technology Facilities Council, 2011.

[29] T. Connolley, C. M. Beavers, and P. Chater, Synchrotron Radiat. News **33**, 31 (2020).

[30] M. Basham, J. Filik, M. T. Wharmby, P. C. Y. Chang, B. El Kassaby, M. Gerring, J. Aishima, K. Levik, B. C. A. Pulford, I. Sikharulidze, D. Sneddon, M. Webber, S. S. Dhesi, F. Maccherozzi, O. Svensson, S. Brockhauser, G. Náray, and A. W. Ashton, J. Synchrotron Radiat. **22**, 853 (2015).

[31] M. G. Tucker, D. A. Keen, M. T. Dove, A. L. Goodwin, and Q. Hui, J. Phys.: Condens. Matter **19**, 335218 (2007).

[32] T. Wakita and M. Yashima, Acta Crystallogr., Sect. B: Struct. Sci., Cryst. Eng. Mater. **63**, 384 (2007).

[33] S. Luo, M. Li, V. Fung, B. G. Sumpter, J. Liu, Z. Wu, and K. Page, Chem. Mater. **33**, 3959 (2021).

[34] E. Mamontov, T. Egami, R. Brezny, M. Koranne, and S. Tyagi, J. Phys. Chem. B **104**, 11110 (2000).

[35] C. Andriopoulou, A. Trimpalis, K. C. Petallidou, A. Sgoura, A. M. Efstathiou, and S. Boghosian, J. Phys. Chem. C **121**, 7931 (2017).

19 January 2024 15:49:14